Effect of asymmetric secondary emission in bounded low-collisional E × B plasma on sheath and plasma properties

Article *in* Journal of Physics D Applied Physics · September 2014

DOI: 10.1088/0022-3727/47/40/405204

CITATIONS
2

READS
89

4 authors, including:

Igor Kaganovich
Princeton University
321 PUBLICATIONS **2,587** CITATIONS

SEE PROFILE

Effect of Asymmetric Secondary Emission in Bounded Low-Collisional E×B Plasma on Sheath and Plasma Properties

Hongyue Wang[1,2], Michael D. Campanell[2], Igor D. Kaganovich[2], Guobiao Cai[1]

[1] Beijing University of Aeronautics and Astronautics, Beijing, 10091, China
[2] Princeton Plasma Physics Laboratory, Princeton, NJ 08543, USA

E-mail: wanghongyue@sa.buaa.edu.cn

Abstract. In a weakly-collisional bounded plasma, secondary electrons emitted from the walls can transit the plasma gap and reach the opposite wall. To accurately predict wall potentials and energy fluxes, one must account for this effect in the flux balance. We present 1D3V particle-in-cell simulations of a plasma slab in an E×B field where the emission yield is different at each wall and varied in a wide parameter range.Analytical formulas are derived to explain the dependence of wall potentials on the emission from both walls. When emission yields are asymmetric, wall with weaker emission charges more negatively to compensate the emission imbalance. We show that small imbalance of emission can lead to relatively large wall potential changes. Moreover, details of secondary electron emission energy distribution are important to take into account for correct calculation of this effect; for example, a small fraction of energetic elastically backscattered secondary electrons can further enhance the wall potential difference. Both walls are usually negative charged by plasma. But for certain magnitudes of the E×B field, a distinct state appears with a positive surface charge at one wall and a negative surface charge at the other, causing a drastic change in the plasma properties.

1. Introduction

It is well known that the electron emission plays an important role in the formation of plasma sheath. The sheath structure in front of one isolated surface were studied making use of fluid [1, 2] and kinetic approaches [3–6]. These studies revealed that the electron emission considerably affects the ion and electron flux balance at the wall and leads to reduction of the sheath potential drop. However, in many low-collisional plasma devices where the electron mean free path exceeds the plasma gap, the electron emitted from one wall can penetrate through the plasma and exit to the opposite wall without undergoing collisions. Thus electron emission can directly affect the net charge flux on walls that are far from their origin, and therefore the formation of sheaths at surfaces bounding the plasma become coupled. This phenomenon exists commonly in the weakly-collisional plasmas. For example, in dc-augmented capacitively coupled plasmas, the ion-induced secondary electrons from the electrode can strike the substrate or the opposite electrode and have a profound effect on the discharge efficiency [7]. The photoelectrons or secondary electrons from the lunar surfaces can reach the lunar orbiter [8], or dominate the charging of the lunar dust grains [9]. In this paper we focus on another typical example: the secondary electrons emission (SEE) in an E×B device. The devices based on E×B drift [10] have been commonly used in plasma immersion ion implantation [11], magnetron discharge [12–15], Penning discharge [16–20], and the Hall thruster [21]. The electron temperature in these devices can reach 20∼50 eV, which is high enough to cause strong electron-induced SEE [22]. The typical electron mean free path can be as long as several meters, while the width of the discharge gap, L is usually several centimeters. Thus the collisionality is low, and a change in SEE flux from one wall can therefore affect charging of the opposite wall.

Another consequence of low-collisionality is the formation of complex electron velocity distribution function (EVDF). In these discharges the EVDF is anisotropic and has a depleted tail as compared to a Maxwellian EVDF; this enhances the effect of SEE recollection by opposite walls on wall charging. Meezan and Cappelli showed in reference [23] that the walls preferentially absorbs fast electrons, therefore high energy tail of EVDF is depleted. Authors of reference [24] showed that the EVDF consists of two components: the secondary electrons emitted from the walls and plasma "bulk" electrons trapped by the potential well formed between two walls, as shown in figure 1. Even though bulk electrons are in the majority, their contribution to the electron flux hitting the wall can be much smaller than secondary electrons from the opposite wall due to the depletion of their EVDF in the high-energy region [24]. Any electron with kinetic energy towards the wall higher than wall potential quickly escapes from the plasma, which leads to depletion of high-energy region of EVDF. In weakly-collisional plasma, the depletion of EVDF cannot be restored by electron elastic collisions, because the scattering is infrequent. Thus the flux of bulk electrons hitting the wall at a given value of wall potential and plasma parameters greatly decreases as compared to the case when the electron mean free path is small compared to the discharge gap. In self-consistent

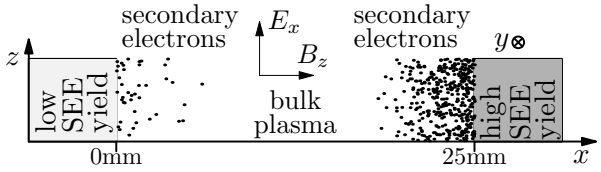

Figure 1. Schematic of the 1D model of E×B discharge.

calculation the electron flux must balance the ion flux, therefore the wall potential in weakly-collisional plasma is typically small compared to the higher pressure plasma when the electron mean free path is small compared to the discharge gap [24]. Moreover, the EVDF of bulk electrons is highly anisotropic. In the y-z plane bulk electrons are accelerated by E×B field; anomalous and collisional scattering processes lead to heating. The EVDF in the y-z plane is approximately a Maxwellian with a temperature T_{ez}. The EVDF in x-direction is no longer Maxwellian due to the depletion at energies that correspond to fast wall losses, so-called loss cone [24]. For electrons with low energies that cannot escape to the wall, the EVDF in direction normal to the wall (x-direction) is approximately also a Maxwellian, but with a temperature T_{ex}, few times less than T_{ez}. A series of particle-in-cell (PIC) simulation has been performed by D. Sydorenko to study details of depletion and anisotropy of EVDF in Hall thruster [25–27]. In electron-neutral collisions, the velocity direction changes and kinetic energy of bulk electrons can be transferred from the y-z plane to the x-direction. Because this scattering process is infrequent in weakly-collisional plasma, only a small portion of bulk electrons can reach the wall due to the scattering by collisions. Unlike bulk electrons, a substantial portion of secondary electrons can penetrate the potential well, because they are emitted from the negatively charged surfaces and accelerated by the sheath and plasma potential to the energy above the potential energy confining electrons (above wall potential times electron charge).

Several investigations have been performed to analyze the effects of secondaries on plasma. Ahedo and Parra developed a fluid model in order to analyze the effect of partial trapping of secondary electrons on the sheath [28]. Assuming part of SEE beams are thermalized by collisions within the bulk plasma, he determined that the sheath potential drop depends mainly on the net SEE current crossing the sheath. Morozov [29] proposed that the secondary electrons can contribute to additional axial electron current and cross magnetic field conductivity, so called near-wall conductivity. This phenomenon was later analyzed in a series of papers based on the fluid model [30], the kinetic theory [31,32] or the PIC numerical simulation [32–34]. Keidar and Beilis [35] described a possible reason for the reduction of near wall conductivity: if the angle between the magnetic field line and the normal of the wall is large, some secondary electrons will return back to the surface within their first gyroration. There is, however, another mechanism for the recollection of secondary electrons back the wall that was seldom analyzed until recently: the asymmetry of the SEE yield of the walls. In Hall thruster, this SEE yield asymmetry can be caused by specially designed wall materials [36–38] or

the wall erosion, which leads to modification of surface roughness [39] that may greatly affects the SEE yield [40]. SEE yield asymmetry leads to asymmetric surface charging and correspondingly potential difference of the two walls forms. Therefore, a large proportion of secondary (and bulk) electrons can be reflected back to the wall before they can reach the opposite wall with higher negative surface charge. Change of SEE yield can lead to drastic changes in sheath structure. For example, if the SEE yield of one wall exceeds unity whereas at another wall is less than one, a regular sheath forms at the wall with small SEE yield and inverse sheath may form at the wall with large SEE yield. Inverse sheath differs from regular sheath in the way electric field accelerates the ions: ions are accelerated towards the wall in regular sheath and decelerated in the inverse sheath [41]. Taccogna observed some of these effects making use of particle-in-cell simulations [34, 42, 43]. Lafleur [44] developed a 1D analytic model to show that a dc bias voltage may form in CCP plasmas due to different ion-induced secondary emission coefficients at each of the rf electrodes; however, the model was based on the assumption of collisional plasma and thus not directly suitable for the weakly-collisional case considered here. Our former work showed that transiting secondaries have a major influence on the wall potential and plasma-surface interaction processes by comparing how flux balance differs in discharges where the secondaries thermalize in the plasma volume from the plasmas where secondaries can propagate through the gap and reach the opposite wall [45]. Because of the importance of this transit effect, one must give a quantitative analysis of the all flux components taking into account secondary electrons from the two walls in order to develop model for the wall potentials, particle and heat fluxes to the walls. That is the aim of this paper.

In this paper, we performed particle-in-cell simulations of plasmas in E×B discharges using a 1D3V-PIC code, EDIPIC [25]. In addition, analytic relations have been derived for wall potentials as a function of the walls SEE yields. This paper is organized as follows: section 2 describes the 1D3V model and the simulation setup. Section 3 presents an overview of the simulation results and the discussions of basic mechanisms of the current balance at the two walls. Section 4 discusses details of the formation of bulk and SEE electrons populations, and gives derivation of the analytical relation between wall potential and SEE yields. Section 5 discusses a limiting case of SEE asymmetry with an inverse sheath at one wall. Finally, the conclusion is offered in section 6.

2. Description of the model

Schematic of the 1D3V simulation model is shown in figure 1. An external constant E×B field was applied to a plasma slab bounded by two infinite plane walls with separately adjustable SEE yield functions. Electrons are magnetized and their motion in all three directions is considered. In all simulation cases the ions are Xe^+. For magnetic field values studied here, ions are not magnetized and only ion motion in direction normal to the wall (x-direction) is taken into account. In x-direction, the potential distribution

Table 1. Initial plasma parameters in the PIC simulation.

Parameter	Symbol	Value
magnetic field (G)	B_x	100
electric field (V/cm)	E_z	100 or 50
width of the plasma slab (mm)	L	25
plasma density (m^{-3})	n	10^{17}
ion temperature (eV)	T_i	1
electron temperature (eV)	T_e	1
neutral density (m^{-3})	n_a	10^{18}
turbulent frequency (Hz)	ν_t	2.8×10^6 (case 1∼4,6) or 7.0×10^6 (case 5)
temperature of the true secondary electron (eV)	T_t	2

and particle dynamics is self-consistently solved. When solving the Poisson equation the potential of the right wall was set to be zero; however, we replotted the potential profiles with zero potential at the centre of the plasma in order to compare the sheath potential values for different simulation cases.

Monte Carlo method was implemented for electron-neutral elastic collisions and ionization collisions between electrons and xenon neutrals in the code. The collision frequencies are calculated as a function of electron energy for given cross sections of these processes [25]. The average collision frequencies of the whole computational region obtained in each simulation case are given in table 3. Additionally, the turbulent collisions are introduced, which randomly scatter particles in y-z plane without changing their energy. It is used to describe the anomalous electron mobility caused by random field fluctuations [25].

Initial parameters of the PIC simulation are listed in table 1. We chose the electric field magnitude below 100V/cm to avoid regimes with relaxation sheath oscillations that complicate analysis [46].

The SEE yield at the walls was based on a SEE yield model of the boron nitride (BN) ceramics, except for the case 4, where the SEE yield was set to be constant as a function of incident electron energy. Details of the SEE yields of boron nitride can be found in reference [25]. Two additional factors, c^L and c^H, are introduced to adjust the SEE yields and establish the asymmetry:

$$\begin{aligned} \gamma^L_{e,s} &= c^L\ \gamma^{BN}(w_e, \theta), \\ \gamma^H_{e,s} &= c^H\ \gamma^{BN}(w_e, \theta), \end{aligned} \tag{1}$$

where, $\gamma^L_{e,s}$ and $\gamma^H_{e,s}$ are respectively the SEE yield for the low-SEE and high-SEE sides. γ^{BN} is analytical model of the SEE coefficient of BN ceramics. Its value depends mainly on the incident electron kinetic energy w_e and weakly on the electron incident angle θ. The secondary electrons emitted from the walls consist of the elastically or inelastically backscattered electrons with energy comparable with incident electron energy and the "true" secondary electrons with energy of few electronvolts. Figure 2 shows the dependence of the total and partial SEE yields on the electron energy w_e

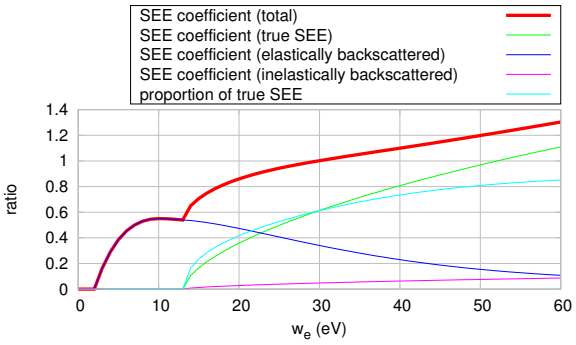

Figure 2. Dependence of the total and partial secondary electron emission yields on the electron energy for the normal incidence [25].

for normal incidence. The angular distribution of secondary electrons is assumed to be axisymmetric with respect to azimuthal angle and proportional to the cosine of the polar angle θ, and independent of the primary electron angle of incidence [25]. The energy of elastically reflected electrons doesn't change after the collisions with the wall. The energy of inelastically backscattered electrons is uniformly distributed between 0 and the energy before the collision. The typical energy distribution curve of true secondary electrons has a peak at about 1∼2eV and decreases rapidly as the energy increases [47]. Here, for simplicity, the electron energy distribution function of secondary electrons is described by a half-Maxwellian distribution:

$$f_w^t(w) = 2\sqrt{\frac{w}{\pi}}\left(\frac{1}{T_t}\right)^{\frac{3}{2}} exp\left(-\frac{w}{T_t}\right) \ . \tag{2}$$

In order to investigate effects of asymmetry of SEE yields on plasma parameters we performed simulations for 6 cases with different values of applied electric field and SEE parameters, as shown in table 2. In some cases SEE was turned off for one or two walls. Cases 1 to 5 focus on the regular sheath. In case 1 to 4 the electric field value was fixed to be 100V/cm, while the SEE yields were varied. In cases 1 and 2 the SEE yields were set to be symmetric, but in case 2 the emission yields were reduced to zero for both walls. In case 3, γ^{BN} was directly used as the SEE yield of the right wall, while for the left side c^L was proportionally reduced from 1 (at 20000 ns) to 0 (at 40000 ns), and the system changed from a symmetric one to a highly-asymmetric one with no emission from the left wall. In case 4 the electron backscattering was not taking into account and all emitted electrons are true secondaries of low energy. The SEE yield of case 4 did not follow the model of BN ceramics but was set to be constant for all incident electron energies with the value corresponding to the net SEE yield of the right wall for the case 3. In case 5 the electric field E was reduced from 100V/cm to 50V/cm. In case 6, the right SEE yield was increased above unity to cause formation of an inverse sheath.

Table 2. The electric field and the SEE model used in the simulations.

case	E_z (V/cm)	left SEE coefficient	right SEE coefficient
1	100	γ^{BN}	γ^{BN}
2	100	0	0
3	100	$c^L\gamma^{BN}$, c^L decreases from 1 to 0	γ^{BN}
4	100	0	0.85 ("true" secondary emission only)
5	50	0	γ^{BN}
6	100	0	$c^H\gamma^{BN}$, $c^H = 1.5$

3. Overview of the simulation results and the discussions of basic mechanisms of the current balance at the two walls.

Taking SEE into account, the current balance at a floating wall reads

$$\Gamma_i \;=\; \Gamma_e \;=\; \Gamma_{e,in} - \Gamma_{e,out} \;=\; (1-\gamma)\Gamma_{e,in}\ , \tag{3}$$

where Γ_e and Γ_i are the net electron and ion fluxes absorbed by the wall, respectively. $\Gamma_{e,in}$ and $\Gamma_{e,out}$ denote the primary and secondary electron flux. In equation (3) γ denotes net or averaged secondary electron emission yield over all electrons incident upon the wall.

In sections 3 and 4 it is assumed that a sheath with negative surface charge on the wall forms, and the coefficients of emission from left or right walls are below unity. And all emitted electrons can pass through the sheath. However, when emission is intensive and secondary electron emission coefficient of plasma electrons incident upon wall exceeds unity, the surface charge can become positive and then a small potential barrier forms to reflect part of secondary electrons back to the wall. Then, the classical Debye sheath becomes a space-charge-limiting sheath [46,48], or an inverse sheath [41,49] forms. An example of the inverse sheath is discussed in section 5 for the limiting case of high SEE asymmetry.

The ion flux Γ_i can be estimated making use of the Bohm criterion for the ion velocity, and the fact that ion number density decreases about twice from the plasma center to the sheath boundary in the collisionless plasma [50]. Note that reference [51] shows Bohm criterion is weakly affected by the presence of electron emission. Therefore one obtains for the ion flux

$$\Gamma_i \;=\; \frac{1}{2} n_e \sqrt{\frac{T_{ex}}{m_i}}\ . \tag{4}$$

It is evident from equation (4) that the ion flux is independent of the sheath potential and is the same for both walls. An apparent consequence from equations (3) and (4) is that the net electrons fluxes Γ_e hitting both floating walls are approximately the same for either symmetric or asymmetric configuration [45]:

$$\Gamma^L_{e,in}\left(1-\gamma^L\right) \;=\; \Gamma^H_{e,in}\left(1-\gamma^H\right)\ . \tag{5}$$

Table 3. The plasma parameters obtained in simulations and corresponding theoretical predictions.

	case number	1	2	3	4	5	6
input variables	E_z(V/cm)	100	100	100	100	50	100
	backscattering	on	on	on	off	on	on
Simulation results	γ^L	0.82	0	0.82−0	0	0	0
	γ^H	0.82	0	0.82−0.86	0.85	0.75	1.0
	T_{ez}(eV)	32.5	37.6	32.5−31.8	29.6	21.8	8
	T_{ex}(eV)	9.5	9.6	9.5−9.4	9.4	7.5	8
	T_{bs}(eV)	10	10	10	NA	6.2	12
	$\nu_{en}(10^5 s^{-1})$	5.3	5.3	5.3	5.3	5.3	5.9
	$\nu_{ioniz}(10^5 s^{-1})$	1.1	1.1	1.1	1.1	1.1	0.3
	$\Phi_p - \Phi_w^H$(V)	18.7	21.4	18.7−18.2	16.7	15.2	1.3
	$\Phi_d = \Phi_w^L - \Phi_w^H$(V)	0	0	0−17.3	6.0	9.9	44.9
	χ_t	0.53	0.53	0.53	1.0	0.53	0.37
Theoretical prediction	$\Phi_p - \Phi_w^H$(V)	15.2	17.3	15.2−15.0	14.0	12.74	NA
	$\Phi_d = \Phi_w^H - \Phi_w^L$(V)	0	0	0−18.7	6.7	11.67	47.7

Here again the superscript 'L' or 'H' respectively denotes the wall with lower or higher SEE. The sheath potential drop is controlled by $\Gamma_{e,in}$ and γ; and if SEE is asymmetric so are incident electron fluxes. Because SEE electrons are propagating through the plasma and are incident on the opposite walls, the two sheaths are coupled to each other due to the SEE electrons transit from one wall to another.

The simulation results for the plasma potential and potential difference between the two walls are summarized in table 3 together with other plasma parameters. The potential profiles for the cases 1-3 are compared in figure 3. For the symmetric cases 1 and 2 (the red and green curves, respectively), the sheath potential drop of both sides increases slightly from 18V to 21V as both SEE yields drop to 0. The potential profile of the highly-asymmetric case 3 without taking emission from the left wall into account is shown by the blue curve. Under this condition, the value of the right sheath potential drop is approximately equal to that for the two symmetric cases. However, the left sheath potential drop greatly increases and the potential structure becomes significantly asymmetric. Figure 4 shows the number density distribution of ions and electrons in the highly-asymmetric case 3. The decrease of electron density in the left sheath corresponds to higher potential drop in the sheath that blocks electrons from reaching the left wall. The sheath width is detected to be about 0.65mm. The evolution of wall potential for the asymmetric case (case 3) is shown in figure 5. As the left SEE coefficient reduces from 0.82 to 0, the sheath potential drop at the right wall remains almost the same, 18V, whereas the value for the left sheath potential drop greatly increases from 18V to 35V.

By examining figure 3 and figure 5, it is evident that the change in wall potential due to variation of SEE yield is obtained only in the asymmetric SEE case, while in the

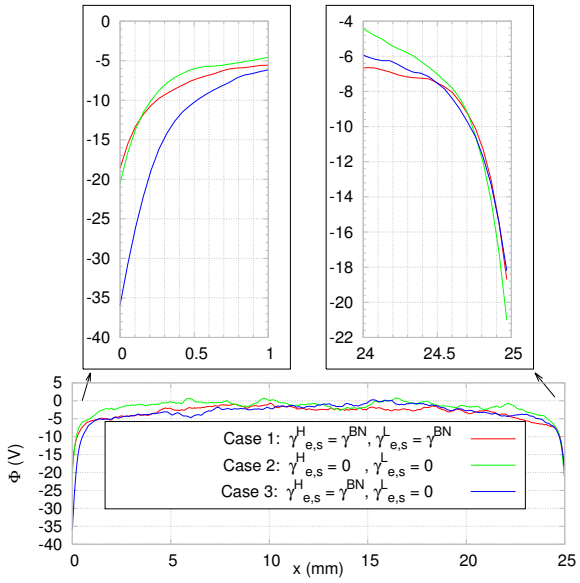

Figure 3. Potential profiles obtained in particle-in-cell simulations (case 1-3.)

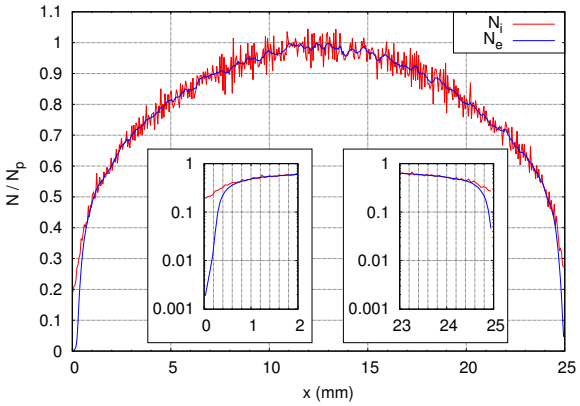

Figure 4. Ion and electron number density profiles obtained in particle-in-cell simulations (case 3, $\gamma^H_{e,s} = \gamma^{BN}$, $\gamma^L_{e,s} = 0$). The data is normalized by the plasma number density at the middle of the channel.

symmetric case the wall potential doesn't change much even if both of the two walls SEE yields are reduced to zero. In the symmetric case, the fluxes of two transiting beams cancel each other on the two walls and, therefore, they don't contribute to the total electron-ion flux ballance; that is why the SEE yield doesn't affect much the wall potential. However, the asymmetry of SEE can break the equality of two counter propagating beam fluxes, and the wall charging process becomes much more complex. In case 3, when the left SEE yield starts to decrease, the net electron flux on the left wall temporally exceeds the ion flux; consequently, the negative charge accumulates on the left surface and the left wall potential drops. The decrease of the left wall potential is

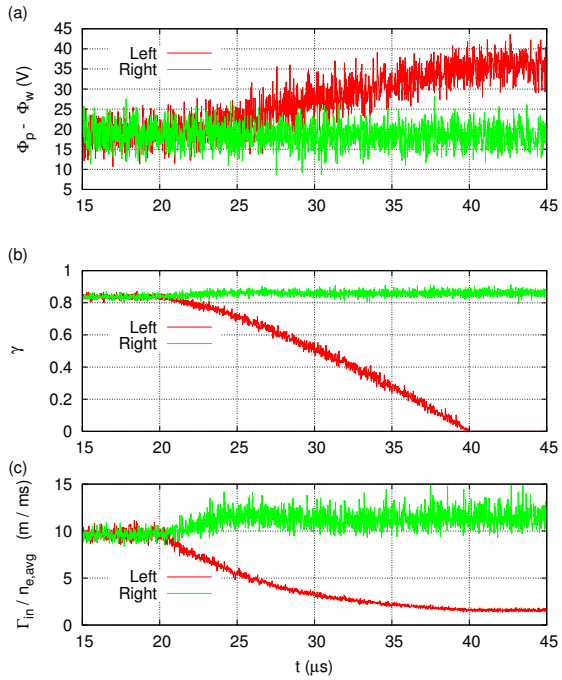

Figure 5. Time-dependant evolution of (a) sheath potential, (b) SEE yields and (c) normalized incident electron flux hitting the two walls in case 3. The electron influx is normalized by the average electron number density $n_{e,avg}$ across the channel.

stopped eventually due to reduction of the electron flux reaching the left wall, as shown in figure 5(c). This rebalance of particle fluxes on the wall is accomplished by reflecting part of incident electrons whose kinetic energy in x-direction is not sufficient to overcome the left sheath and reach the wall. Figure 6 illustrates different components of electron fluxes in an asymmetric SEE system. The electron flux hitting the right wall includes 4 components. Two of them, the collision-ejected (CE) electrons which are bulk electrons scattered by collisions with neutrals (denoted by the subscript 'ce' in this paper) and the SEE electrons ejected by the opposite wall (denoted by the subscript 'b' for beam), also exist in the symmetric case, see reference [24] for details. However, the SEE asymmetry creates two additional components: the beam electrons or bulk electrons reflected by the stronger left sheath (denoted in the paper by the subscript 'rb' and 'rce'). Thus the incident electron flux to the right wall is the sum of 4 components:

$$\Gamma^H_{e,in} = \Gamma^H_b + \Gamma^H_{rb} + \Gamma^H_{ce} + \Gamma^H_{rce} , \tag{6}$$

$$\Gamma^L_{e,in} = \Gamma^L_b + \Gamma^L_{ce} . \tag{7}$$

In order to describe the complex process of penetration, trapping and reflection of electrons between two walls, two additional penetration ratios are introduced, defined as follows:

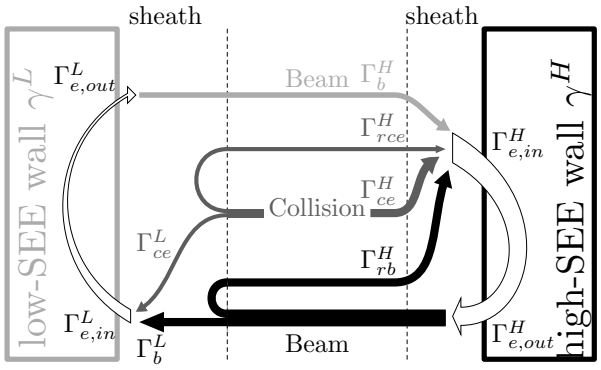

Figure 6. Schematic of the electron flux equilibrium between the two walls with two negatively sheaths. The width of the sheath is exaggerated.

$$\alpha^b = \frac{\Gamma^L_b}{\Gamma^H_{e,out}} , \tag{8}$$

$$\alpha^{ce} = \frac{\Gamma^L_{ce}}{(\Gamma^H_{rce} + \Gamma^L_{ce})} = \frac{\Gamma^L_{ce}}{\Gamma^H_{ce}} . \tag{9}$$

Here, α^b is the fraction of electrons emitted by the right wall that can reach the left wall. α^{ce} is the ratio of collision-ejected fluxes incident on left and right walls. $\alpha^{ce} < 1$ because sheath potential drop is higher for the left wall. α^{ce} also measures the reflection of collision-ejected electrons by the left sheath. The scattering of electrons in the electron-neutral collision is random, thus the flux of electrons that initially move towards the two walls must be equal. Therefore one obtains

$$\alpha^{ce} = \left(1 + \frac{\Gamma^H_{rce}}{\Gamma^L_{ce}}\right)^{-1} . \tag{10}$$

The description of α^{ce} and the collision ejected electron dynamics is further explained in section 4.

Substituting equations (6)-(8) into equation (5) yield a relation between the penetration ratios and the secondary emission coefficients:

$$(1 - \alpha^{ce}) + \frac{\gamma^L}{1 - \gamma^L} = \alpha^b \frac{\gamma^H}{1 - \gamma^H} . \tag{11}$$

The two penetration ratios, α_{ce} and α_b, are both dependant on the potential difference between two walls $\Phi_d = \Phi^L_w - \Phi^H_w$, therefore equation (11) is equation for the potential difference between two walls.

4. The analytical relation between the wall potentials and SEE yields

4.1. Bulk electrons

In the asymmetric case, the bulk electrons consist of 3 groups dependent on x-directional kinetic energy, w_x, and the potential at the location of the electron, $\Phi(x)$. Electrons

with w_x less than $e|\Phi(x) - \Phi_w^H|$ are trapped between two sheaths. Electrons with $w_x > e|\Phi(x) - \Phi_w^L|$ can penetrate both sheaths and escape to either wall. Therefore, the electron fluxes hitting the two walls are the same for this group. Electrons with $e|\Phi(x) - \Phi_w^H| < w_x < e|\Phi(x) - \Phi_w^L|$ can penetrate only the right sheath, and those moving towards left are reflected by the left sheath, doubling the bulk electron influx towards the right wall in this energy range.

The right sheath at the high-SEE wall controls the electron-ion flux equilibrium on the whole systems, because the potential barrier at this wall for electrons to escape is lowest. As discussed above, the emitted electrons in very weakly collisional system transit between walls, therefore they do not contribute to total electron flux to two walls. Therefore balance of electron and ion fluxes on two walls gives

$$\Gamma_{ce}^H + \Gamma_{ce}^L + \Gamma_{rce}^H \;=\; 2\Gamma_{ce}^H \;=\; 2\Gamma_i \;. \tag{12}$$

As previously mentioned, the ion flux is not affected by the sheath, consequently, the sum of bulk electron fluxes doesn't change if one of SEE yields is changed according to equation (12). Therefore, the smaller (right) sheath potential is not sensitive to secondary emission, as shown in figure 3 and figure 5(a) [45].

It was proved in reference [24] that for the low-collisional plasma with highly anisotropic temperature and depleted EVDF tail, the collision-ejected electrons flux is reduced by a factor of order $L/(2\lambda)$ compared with the value for the isotropic Maxwellian EVDF:

$$\Gamma_{ce} \;\simeq\; \frac{L}{8\lambda} n_e \sqrt{\frac{8T_{ez}}{\pi m_e}} e^{-\frac{e(\Phi_p - \Phi_w)}{T_{ez}}} \;, \tag{13}$$

where T_{ez} is the electron temperature in the direction parallel to the walls. Figure 7 and figure 8 depict simulation results for the highly anisotropic EVDF and electron temperature of case 3 (in both limiting cases: symmetric and asymmetric). In x-direction, the electron temperature $T_{ex} \approx 9.5$eV is much lower compared with $T_{ez} \approx 32$eV, and even in the asymmetric case the EVDF is depleted in both positive and negative region where w_x is larger than the right wall potential 18V. It proves our assumption that part of collision-ejected electrons with $w_x > e|\Phi(x) - \Phi_w^H|$ moving leftward finally propagate through the right sheath after reflection from the left sheath. The z-directional EVDF is close to the Maxwellian distribution with $T_{ez} \approx 32$eV in either symmetric or asymmetric state as shown in figure 8.

Substituting equations (13) and (4) into equation (12) gives the relation for the wall potential at the high-SEE side

$$\Phi_p - \Phi_w^H \;= \frac{T_{ez}}{e} \ln\left[\frac{L}{\lambda}\sqrt{\frac{T_{ez}}{T_{ex}}}\sqrt{\frac{m_i}{2\pi m_e}}\right] \;. \tag{14}$$

The electron free path λ in equation (14) can be estimated from the electron-neutral collision frequency ν_{en} and the average electron speed in the y-z plane $\sqrt{(\pi T_{ez})/(2m_e)}$. Calculated values for the right wall potential given by equation (14) are summarized

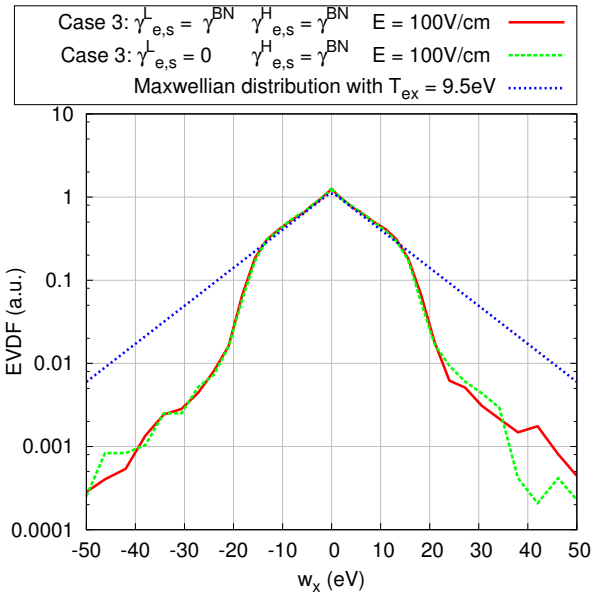

Figure 7. The x-directional EVDF in the middle of the channel of case 3. The red solid line is the simulation result for the symmetric state. The dashed green line is the simulation result for the highly asymmetric state with $\gamma^L = 0$. The data are obtained by sampling in the middle of the channel (between x= 8mm and 17mm). The dotted blue line is the Maxwellian distribution with $T_{ex} = 9.5$eV.

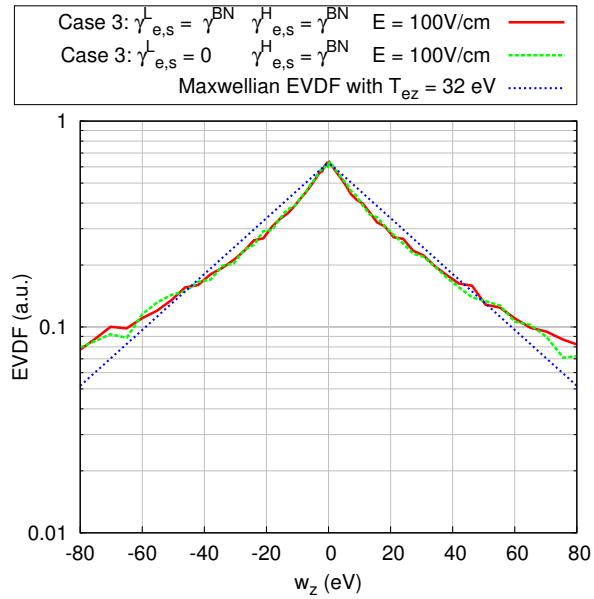

Figure 8. The z-directional EVDF in the middle of the channel of case 3. The red solid line is the simulation result for the symmetric state. The dashed green line is the simulation result for the highly asymmetric state with $\gamma^L = 0$. The data are obtained by sampling in the middle of the channel (between x= 8mm and 17mm). The dotted blue line is the Maxwellian distribution with $T_{ez} = 32$eV.

in table 3. Comparison with the values obtained in simulations 1-5 shows reasonable agreement.

In the asymmetric case, the higher left wall potential reflects bulk and beam electrons with $e|\Phi(x) - \Phi_w^H| < w_x < e|\Phi(x) - \Phi_w^L|$ towards the right wall. Consider limiting asymmetric case with no emission from the left. Multiplying equation (11) by Γ_i and taking $\gamma^L = 0$ and $\Gamma_{e,\ out}^H = \Gamma_i(\gamma^H/1 - \gamma^H)$ gives

$$(1 - \alpha^{ce})\Gamma_{ce}^H \ = \ \alpha^b \Gamma_{e,\ out}^H \ . \tag{15}$$

The right side of equation (15) is the net flux of beam electrons that transit from the right wall to the left wall. The left side of the equation (15) is flux of collision-ejected electrons that is reflected by the left sheath. The bulk electrons are driven by potential asymmetry to move towards right, which partially compensates the electrons carried away from the right wall by beam. The transit of bulk electrons is described by the penetration ratio of bulk electrons α^{ce} that is defined by equation (9). In the symmetric case $\alpha^{ce} = 1$. If the SEE asymmetry develops, α^{ce} decreases because more bulk electrons are transferred to the right wall.

Because the temperature and the mean free path of electrons in equation (13) are not sensitive to SEE, the collision-ejected electron flux is proportional to a function of the sheath potential drop and the temperature of z-direction:

$$\Gamma_{ce} \ \propto \ e^{-\frac{e(\Phi_p - \Phi_w)}{T_{ez}}} \ . \tag{16}$$

Hence the penetration ratio α^{ce} can be derived as:

$$\alpha^{ce} \ = \ \frac{\Gamma_{ce}^L}{\Gamma_{ce}^H} \ = \ \frac{e^{-\frac{e(\Phi_p - \Phi_w^L)}{T_{ez}}}}{e^{-\frac{e(\Phi_p - \Phi_w^H)}{T_{ez}}}} \ = \ e^{-\frac{e\Phi_d}{T_{ez}}} \ . \tag{17}$$

4.2. Beam electrons

A beam electron moving leftwards reaches the opposite wall if its initial energy w_{ex} exceeds the potential difference between the two walls. Thus the penetration ratio α^b can be derived from the initial EVDF of the beam electrons:

$$a^b(\Phi_d) = \frac{\int_{\sqrt{\frac{2e\Phi_d}{m}}}^{\infty} f_v^b(v_{ex}) dv_{ex}}{\int_0^{\infty} f_v^b(v_{ex}) dv_{ex}} \ , \tag{18}$$

where $f_v^b(v_{ex})$ is the initial x-directional EVDF of beam electrons.

It is evident from equation (18), that α^b decreases sharply if Φ_d exceeds typical energy of emitted electrons. As described in section 2, beam electrons consist of two groups: true secondary electrons and backscattered electrons. For backscattered electrons, their energy (of order of incident energy) is much higher than the energy of the true secondary electrons (few eV). Figure 9 illustrated the evolution of the beam electron fluxes of backscattered (elastically and inelastically) and true secondary electrons incident on the left wall for the case 3. The flux of true secondary electrons

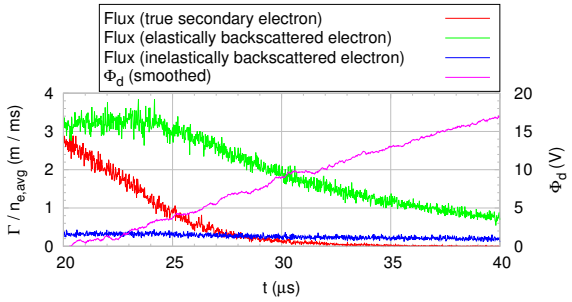

Figure 9. The flux of 3 beam electron components incident on the left wall obtained in the simulation of case 3. The red, green and blue curve are respectively the flux of true secondary, elastically backscattered and inelastically backscattered electrons, which are normalized by average electron number density across the channel $n_{e,avg}$. The magenta curve is smoothed simulation data of potential difference between two walls.

greatly decreases immediately after Φ_d slightly rises above few volts, and diminishes to almost 0 when Φ_d exceeds 10V. But the backscattered electron flux hardly changes when Φ_d is less than 4V. And even though the backscattered electron flux decreases after Φ_d surpasses 4V, it never vanishes. *In fact, as we show below the backscattered electron flux is responsible for high value of* Φ_d.

Based on a specific initial EVDF of the beam, one can derive analytical relation between α^b and Φ_d. Figure 10 shows that the beam EVDF obtained in simulation 3 have two peaks at 1eV and 10eV, which correspond to the x-directional energy of true secondaries and backscattered electrons, respectively. Neglecting small contribution from inelastically scattered electrons, the beam EVDF can be approximated by a two components model. The true secondaries EVDF, described in section 2 reads

$$f^t_{v_x}(v_x) \;=\; \frac{mv_x}{T_t} exp\left(\frac{-mv_x^2}{2T_t}\right) \;. \tag{19}$$

The EVDF of backscattered electrons can also be approximated by equation (19), but with a different temperature T_{bs}, and the total EVDF of the beam becomes

$$f^b_{v_x}(v_x) \;=\; \chi_t \frac{mv_x}{T_t} exp\left(\frac{-mv_x^2}{2T_t}\right) + \chi_{bs} \frac{mv_x}{T_{bs}} exp\left(\frac{-mv_x^2}{2T_{bs}}\right) \;, \tag{20}$$

where T_t and T_{bs} are temperatures of the true secondary electrons and backscattered electrons, and χ_t and χ_{bs} are the proportions of the true secondaries and backscattered electrons in the total emission flux:

$$\chi_t = \frac{\gamma^H_{true}}{\gamma^H} \;,$$
$$\chi_{bs} = 1 - \chi_t \;.$$

T_{bs} depends on the incident energy and is function of T_{ez}, which is governed by the drift speed E_z/B_x. Figure 10 shows that the beam EVDF obtained in the asymmetric state

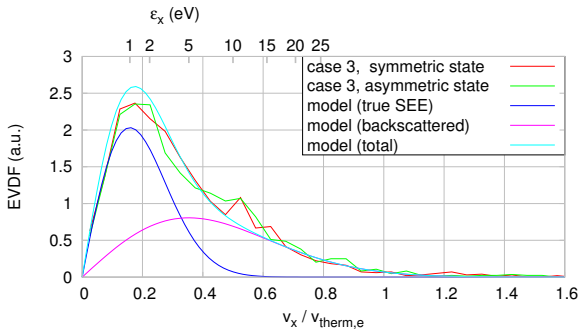

Figure 10. The distribution function of the x-directional velocity of the secondary electrons emitted by the right wall. The x-directional velocity is normalized by a typical speed $v_{therm,e} = 3.75 \times 10^6$ m/s, and the corresponding energy $\varepsilon_x = \frac{1}{2} m_e v_x^2$ is shown at the top axis of the graph. The red and green lines are simulation data of case 3 for the symmetric state and the highly asymmetric state with $\gamma^L = 0$. The cyan line is the approximate model drawn by equation (20). The magenta and blue lines are backscattered and true secondary parts of equation (20).

of case 3 doesn't differ much from the symmetric state, indicating T_{bs} is not sensitive to left SEE yield. Therefore, it is reasonable to use a constant value for T_{bs} in all cases with $E_z = 100V/cm$ and choose a smaller value for the case 5 with $E_z = 50V/cm$. Then T_{bs} was obtained to be 10eV for case 1 and 3 to fit the simulation data of the beam EVDF, and 6.2eV for case 5.

Incident electron creates one or more "true" secondary electrons only if its energy exceeds 13eV as shown in figure 2. χ_t is found to be around 0.5 in case 1, 3 and 5. In case 4 electron backscattering is shut down thus $\chi_t = 1$. The inelastically backscattered electrons are ignored because its partial emission yield is quite small. This approximate model of beam EVDF is compared with the simulation data in figure 10. From equations (18) and (20) one finally obtains the beam penetration ratio α^b:

$$\alpha^b(\Phi_d) = \chi_t \; exp\left(-\frac{e\Phi_d}{T_t}\right) + \chi_{bs} \; exp\left(-\frac{e\Phi_d}{T_{bs}}\right) \; . \tag{21}$$

4.3. Final equation of the wall potential

Substituting equations (17) and (21) into equation (11) gives the relation between SEE yields and the potential difference between walls, Φ_d:

$$\frac{1}{1-\gamma^L} = \frac{\gamma^H}{1-\gamma^H}\left[\chi_t \; exp\left(-\frac{e\Phi_d}{T_t}\right) + \chi_{bs} \; exp\left(-\frac{e\Phi_d}{T_{bs}}\right)\right] + exp\left(-\frac{e\Phi_d}{T_{ez}}\right). \tag{22}$$

When $\Phi_d = 0$ equation (22) reduces to a simple equation $\gamma^L = \gamma^H$ that reflects the symmetry of SEE. Table 3 compares the solution for Φ_d given by equation (22) with the simulation result of cases 1-5 and shows an good agreement.

Figure 11 plots the analytical (the green line) and simulation results (the red line) of Φ_d in case 3. When solving equation (22) for case 3, the time-dependant evolution of

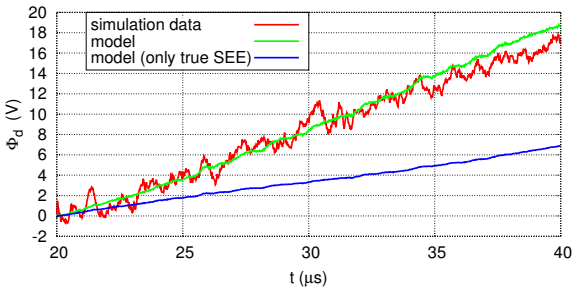

Figure 11. The time-dependent evolution of Φ_d obtained by the simulation of case 3 and the analytical model of equation (22). The red curve is the simulation result. The green curve is calculated by equation (22) using simulation data of SEE yields as input parameters, with $T_{bs} = 10$eV, $T_{ez} = 32$eV and $\chi_t = 0.53$. The blue curve is calculated by the similar approach of the green curve except that $\chi_t = 1$. All the three curves were smoothed by averaging 25 adjacent data points.

SEE coefficients obtained in the simulation were used as input parameters at each time point. Equation (22) reveals that Φ_d increases with γ^H or with reducing γ^L, therefore Φ_d increases quickly when the asymmetry of emission coefficients develops. The blue line in figure 11 show analytical prediction for Φ_d when backscattering is not taken into account. From figure 11 it is evident that backscattered electrons with much higher energy significantly affect charging of the left wall. A comparison between the potential profiles obtained in simulation case 3 and 4 also demonstrates this effect, as shown in figure 12.

Examining the results for the case 3 and 5 in table 3 and in figure 13, it is evident that the electric field E_z, or drift speed E_z/B_x, affects Φ_d by controlling the temperature of bulk electrons T_{ez}. When E_z reduces from 100V/cm to 50V/cm, T_{ez} reduces from 32eV to 22eV. The change of T_{ez} also leads to a decrease of backscattering electron temperature T_{bs}. Thus the value of Φ_d is much smaller in case 5 compared with that of the case 3 where the left SEE yield is negligibly small, as predicted by equation (22).

Even though discussion in sections 3 and 4 was limited to electron-induced secondary electron emission, other effects such as ion-induced secondary emission or formation of negative ions at the wall can be easily included in the model.

5. The unilateral inverse sheath

In this section we discuss limiting case of SEE asymmetry in which one of the two emission coefficients surpasses 1. Figure 14 shows the potential profiles of case 6 (the red line) where the right SEE yield was chosen to be 1.5 times that of BN and no emission from the left wall. An inverse sheath [41] appears near the right wall with a small potential increase of 1V. The left wall potential is still negative with a potential drop of 45V that is much larger than the maximal value of case 3 with the same value of electric field (see the blue line).

A wall potential is required to suppress some of the emission from the right wall,

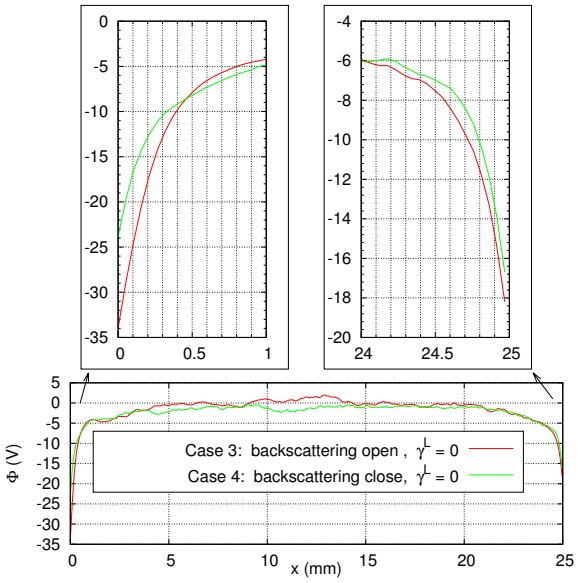

Figure 12. Potential profiles obtained in particle-in-cell simulations (case 3 and 4.)

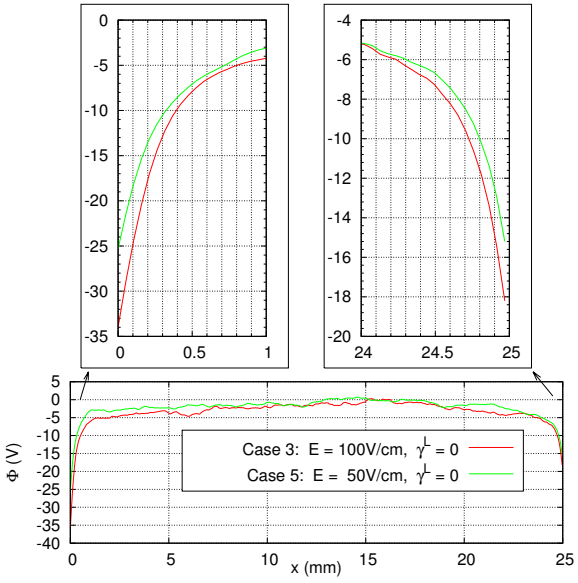

Figure 13. Potential profiles obtained in particle-in-cell simulations (case 3 and 5.)

because net emission from the incident electron flux exceeds unity without sheath potential drop. Figure 15 shows how electrons and ions travel in the unilaterally positive sheath state. Part of secondary electrons emitted by the right wall, named 'near-wall reflected electrons' (NWRE) in this paper, are immediately reflected by the sheath back to the wall. The NWREs' energy is small and their contribution to emission is negligible. Thus the net SEE coefficient of the right wall can be maintained to unity. The ions cannot reach the right wall, because their energy is less than wall potential. Therefore, the charge balance on the right wall is only between incident and secondary

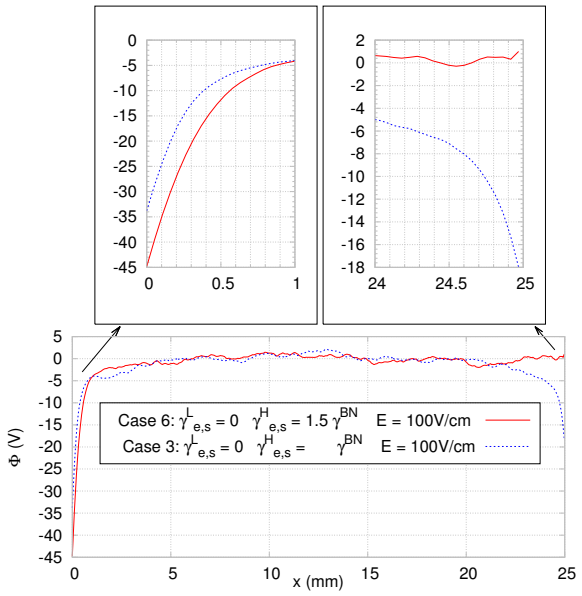

Figure 14. Potential profiles obtained in particle-in-cell simulations (case 3 and 6.)

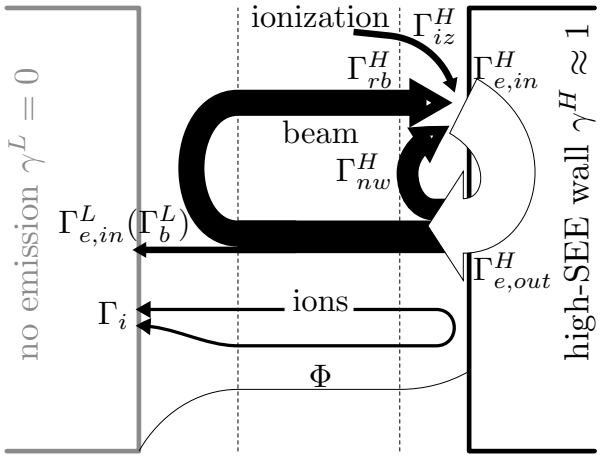

Figure 15. Sketch of the electron and ion flux equilibrium between two walls in the unilaterally positive sheath case. The width of the sheath is exaggerated.

electron fluxes.

In case 6, any bulk electron moving rightward is free to reach the wall and produces secondary electrons. The initial bulk electrons quickly escape and all electrons are former secondaries. Figure 16 presents the x-directional and z-directional EVDF in the middle of the discharge of case 6. At the energy corresponding to the left wall potential, the value of x-directional EVDF curve is less than 0.01. It proves only a tiny minority of electrons can penetrate the left sheath.

In figure 16 we see that the EVDF of case 6 is close to an isotropic Maxwellian distribution with $T_e = 8$eV, except for the depletion of the high-energy region in the positive x-direction. As electrons transit between two walls, the high-energy tail of their x-directional EVDF is cut off due to the electron absorption by the left wall, but it is

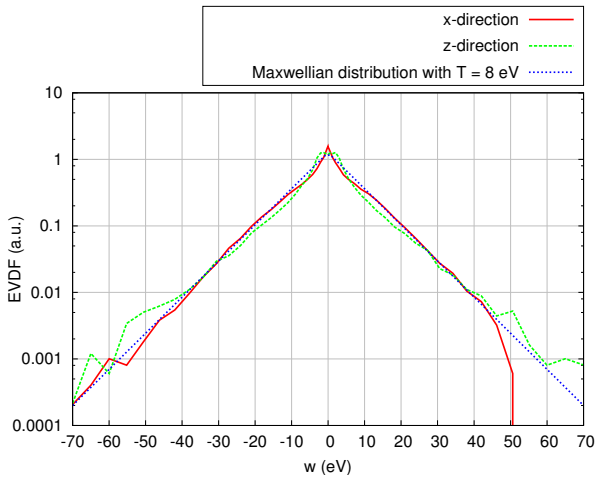

Figure 16. The x-directional and z-directional EVDF in the middle of the channel of case 6. The red solid line is x-directional EVDF. The dashed green line is z-directional EVDF. The data are obtained by sampling in the middle of the channel (between x= 8mm and 17mm). The dotted blue line is the Maxwellian distribution with $T_e = 8$eV.

partially restored by backscattering near the right wall. For case 6 the two electron temperatures in x and z direction T_{ez} and T_{ex} are almost the same, because electron backscattering plays a dominant role in the secondary emission for electron with low energy (see figure 2). In case 6, the partial SEE coefficient of backscattering γ_{bs} is as high as 0.6. T_{ez} can be much higher than T_{ex} if γ_{bs} largely reduces in case of a higher electric field and the incident electron energy. In case of $T_{ex} \approx T_{ez}$, the potential difference between the two walls can be calculated from the balance of ion and electron fluxes and is similar to the potential drop in the collisionless sheath at a floating wall in the semi-infinite Maxwellian plasma slab [52]:

$$\Phi_d^M = \frac{T_{ez}}{e} \ln\left(\xi\sqrt{\frac{m_i}{2\pi m_e}}\right) . \tag{23}$$

Here the factor $\xi = 2$ differs from $\xi = 1$ of the semi-infinite plasma, because the reflection of ions from the right sheath doubles the ion flux at the left wall. Equation (23) gives the upper limit of Φ_d caused by SEE asymmetry. Using parameters of case 6 one can obtain $\Phi_d^M = 47.7$V by equation (23), which agrees well with the simulation result 45V.

6. Conclusion

In this paper we analyzed the electron kinetics in a weakly-collisional plasma slab bounded by two floating walls that emit secondary electrons. It was shown analytically and confirmed by particle-in-cell simulations that, the difference of SEE coefficients between two walls leads to asymmetry of surface charging, sheath structure and wall potential.

In case of two negative wall potentials relative to the plasma, the sheath potential drop of the high-SEE side is not affected by low-SEE secondary emission. We generalized

an analytical relation of the sheath potential for the symmetric SEE [24] to the asymmetric case. The potential drop in the sheath of the low-SEE wall can greatly exceeds the drop in the sheath of the high-SEE wall due to contribution of back scattered electrons.

An unilateral positive wall potential appears when the emission coefficient of the high-SEE wall approaches 1. In this case the electric potential monotonically increases from the low-SEE wall to the high-SEE wall. For the high-SEE side, ions are reflected from the high-SEE wall by the positive potential while all electrons are free to reach that wall and all original bulk electrons escape and are converted to secondary electrons. The low-SEE wall charges negatively to the potential given by formula similar to the semi-infinite plasma

$$\Phi_d^M = \frac{T_{ez}}{e} \ln\left(\xi\sqrt{\frac{m_i}{2\pi m_e}}\right) .$$

Here, the factor $\xi = 2$ differs from $\xi = 1$ of the semi-infinite plasma, because the reflection of ions from the right sheath doubles the ion flux at the left wall. Our results revealed the high-energy tail of EVDF is depleted at the low-SEE wall and then restored by electron backscattering near the high-SEE wall.

Acknowledgments

The authors are indebted to Dmytro Sydorenko, the developer of the EDIPIC code, Alexander V. Khrabrov, and Yevgeny Raitses for valuable discussion. This work was supported in parts by Chinese Scholarship Council and the U.S. Department of Energy.

References

[1] Hobbs G D and Wesson J A 1967 *Plasma Phys.* **9** 85
[2] Ye M and Takamura S 2000 *Phys. Plasmas* **7** 3457
[3] Schwager L A 1993 *Phys. Fluids B* **5** 631–645
[4] Schwager L and Birdsall C 1990 *Phys. Fluids B* **2** 1057
[5] Sheehan J P, Hershkowitz N, Kaganovich I D, Wang H, Raitses Y, Barnat E V, Weatherford B R and Sydorenko D 2013 *Phys. Rev. Lett.* **111** 075002
[6] Gyergyek T and Kovačič J 2012 *Phys. Plasmas* **19** 013506
[7] Kawamura E, Lichtenberg A and Lieberman M 2008 *Plasma Sources Sci. Technol.* **17** 045002
[8] Halekas J, Delory G, Lin R, Stubbs T and Farrell W 2009 *Planet. and Space Sci.* **57** 78
[9] Sickafoose A, Colwell J, Horányi M and Robertson S 2001 *J. Geophys. Res.* **106** 8343
[10] Abolmasov S 2012 *Plasma Sources Sci. Technol.* **21** 035006
[11] Keidar M, Monteiro O, Anders A and Boyd I 2002 *Appl. Phys. Lett.* **81** 1183
[12] Levchenko I, Romanov M, Keidar M and Beilis I 2004 *Appl. Phys. Lett.* **85** 2202
[13] Kolev I and Bogaerts A 2006 *Plasma Process. Polym.* **3** 127
[14] Yusupov M, Bultinck E, Depla D and Bogaerts A 2011 *New J. Phys.* **13** 033018
[15] Bultinck E and Bogaerts A 2011 *Plasma Sources Sci. Technol.* **20** 045013
[16] Knauer W 1962 *J. Appl. Phys.* **33** 2093
[17] Malmberg J and Driscoll C 1980 *Phys. Rev. Lett.* **44** 654
[18] Huang X P, Anderegg F, Hollmann E, Driscoll C and O'neil T 1997 *Phys. Rev. Lett.* **78** 875

[19] Boeuf J P and Chaudhury B 2013 *Phys. Rev. Lett.* **111** 155005
[20] Platonov A, Slyshov A, Tsendin L and Wagner S 2006 *Tech. Phys.* **51** 841
[21] Martinez-Sanchez M and Pollard J 1998 *J. Propul. Power* **14** 688
[22] Raitses Y, Kaganovich I D, Khrabrov A, Sydorenko D, Fisch N J and Smolyakov A 2011 *IEEE Trans. Plasma Sci.* **39** 995
[23] Meezan N B and Cappelli M A 2002 *Phys. Rev. E* **66** 036401
[24] Kaganovich I, Raitses Y, Sydorenko D and Smolyakov A 2007 *Phys. Plasmas* **14** 057104
[25] Sydorenko D 2006 *Particle-in-cell simulations of electron dynamics in low pressure discharges with magnetic fields* Ph.D. thesis University of Saskatchewan
[26] Sydorenko D, Smolyakov A, Kaganovich I and Raitses Y 2006 *Phys. Plasmas* **13** 014501
[27] Sydorenko D, Smolyakov A, Kaganovich I and Raitses Y 2006 *IEEE Trans. Plasma Sci.* **34** 815
[28] Ahedo E and Parra F 2005 *Phys. Plasmas* **12** 073503
[29] Morozov A and Savel'ev V 2001 *Plasma Phys. Rep.* **27** 570
[30] Barral S, Makowski K, Peradzyński Z, Gascon N and Dudeck M 2003 *Phys. Plasmas* **10** 4137
[31] Degond P 1998 *SIAM J. Appl. Math.* **58** 1138
[32] Ivanov A A, Jr A A I and Bacal M 2002 *Plasma Phys. Contr. F.* **44** 1463
[33] Yu D, Liu H, Cao Y and Fu H 2008 *Contrib. Plasma Phys.* **48** 543
[34] Taccogna F, Longo S, Capitelli M and Schneider R 2008 *Contrib. Plasma Phys.* **48** 375
[35] Keidar M and Beilis I I 2009 *Appl. Phys. Lett.* **94** 191501
[36] Fisch N, Raitses Y, Dorf L and Litvak A 2001 *J. Appl. Phys.* **89** 2040
[37] Raitses Y, Keidar M, Staack D and Fisch N 2002 *J. Appl. Phys.* **92** 4906
[38] Raitses Y, Staack D and Fisch N 2008 *IEEE T. Plasma Sci.* **36** 1202
[39] Zidar D G and Rovey J L 2012 *J. Propul. Power* **28** 334
[40] Pivi M, King F, Kirby R, Raubenheimer T, Stupakov G and Le Pimpec F 2008 *J. Appl. Phys.* **104** 104904
[41] Campanell M, Khrabrov A and Kaganovich I 2012 *Phys. Rev. Lett.* **108** 255001
[42] Taccogna F, Longo S and Capitelli M 2005 *Phys. Plasmas* **12** 093506
[43] Taccogna F, Schneider R, Longo S and Capitelli M Effect of surface roughness on secondary electron emission in a hall discharge *Proc. 42nd AIAA/ASME/SAE/ASEE Joint Propulsion Conf.(Sacramento, AL)* AIAA paper 2006-4662 (American Institute of Aeronautics and Astronautics)
[44] Lafleur T, Chabert P and Booth J 2013 *J. Phys. D: Appl. Phys.* **46** 135201
[45] Campanell M and Wang H 2013 *Appl. Phys. Lett.* **103** 104104
[46] Sydorenko D, Kaganovich I, Raitses Y and Smolyakov A 2009 *Phys. Rev. Lett.* **103** 145004
[47] Seiler H 1983 *J. Appl. Phys.* **54** R1
[48] Rozhansky V A and Tsendin L D 2001 *Transport phenomena in partially ionized plasma* (London & New York: Taylor & Francis) p 88
[49] Campanell M 2013 *Phys. Rev. E* **88** 033103
[50] Kaganovich I 2002 *Phys. Plasmas* **9** 4788
[51] Sheehan J, Kaganovich I, Wang H, Sydorenko D, Raitses Y and Hershkowitz N 2014 *Phys. Plasmas* **21** 063502
[52] Lieberman M A and Lichtenberg A J 2005 *Principles of plasma discharges and materials processing* (Hoboken: John Wiley & Sons Inc.) p 172